sion weighting. At relatively low b-values, signal intensity in the isotropic DWI is dominated by fast-diffusing water molecules, whereas at higher b-values, signal intensity is contributed largely by slow-diffusing water molecules. The decrease in ADC observed at higher-b-value DWI in our series may have been somewhat affected by the higher sensitivity to slow-diffusion water molecules. Because many different b-values are necessary for biexponential model fitting, EPI is difficult timewise and line scanning with multiple b settings may be superior. However, the line scanning technique is available only in a limited number of facilities and allows only a limited number of slice locations.[21]

Our study has some limitations. First, our gold standard was biopsy. The size and location of small malignant lesions, which were undetectable on T_2-weighted images and/or gadolinium-enhanced dynamic images, were unclear, and accurate ROI setting for such lesions is not possible. Therefore, we excluded such lesions as malignant lesions. Comparison of the MR results with total histological specimens following radical prostatectomy is required before more realistic conclusions can be drawn. Second, we analyzed normal and malignant tissues in the peripheral zone; future studies will be needed to further consider the transition zone.

Conclusion

ADC measurement using a high (2,000 s/mm²) compared with standard (1,000 s/mm²) b-value in a monoexponential model offers little diagnostic advantage for discriminating malignant from normal prostate tissue under the same imaging conditions.

Acknowledgements

References

1. Quinn M, Babb P. Patterns and trends in prostate cancer incidence. Survival, prevalence and mortality. Part I: international comparisons. BJU Int 2002; 90:162–173.
2. Franceschi S, La Vecchia C. Cancer epidemiology in the elderly. Crit Rev Oncol Hematol 2001; 39: 219–226.
3. Zakian KL, Sircar K, Hricak H, et al. Correlation of proton MR spectroscopic imaging with Gleason score based on step-section pathologic analysis after radical prostatectomy. Radiology 2005; 234: 804–814.
4. Buckley DL, Roberts C, Parker GJ, Logue JP, Hutchinson CE. Prostate cancer: evaluation of vascular characteristics with dynamic contrast-enhanced T_1-weighted MR imaging-initial experience. Radiology 2004; 233:709–715.
5. Gibbs P, Tozer DJ, Liney GP, Turnbull LW. Comparison of quantitative T_2 mapping and diffusion-weighted imaging in the normal and pathologic prostate. Magn Reson Med 2001; 46: 1054–1058.
6. Issa B. *In vivo* measurement of the apparent diffusion coefficient in normal and malignant prostatic tissues using echo-planar imaging. J Magn Reson Imaging 2002; 16:196–200.
7. Chan I, Wells W 3rd, Mulkern RV, et al. Detection of prostate cancer by integration of line-scan diffusion, T_2-mapping and T_2-weighted magnetic resonance imaging: a multichannel statistical classifier. Med Physics 2003; 30:2390–2398.
8. Hosseinzadeh K, Schwarz SD. Endorectal diffusion-weighted imaging in prostate cancer to differentiate malignant and benign peripheral zone tissue. J Magn Reson Imaging 2004; 20:654–661.
9. Sato C, Naganawa S, Nakamura T, et al. Differentiation of noncancerous tissue and cancer lesions by apparent diffusion coefficient values in transition and peripheral zones of the prostate. J Magn Reson Imaging 2005; 21:258–262.
10. Pickles MD, Gibbs P, Sreenivas M, Turnbull LW. Diffusion-weighted imaging of normal and malignant prostate tissue at 3.0T. J Magn Reson Imaging 2006; 23:130–134.
11. Tanimoto A, Nakashima J, Kohno H, Shinmoto H, Kuribayashi S. Prostate cancer screening: The clinical value of diffusion-weighted imaging and dynamic MR imaging in combination with T_2-weighted imaging. J Magn Reson Imaging 2007; 25:146–152.
12. Wiesinger F, Boesiger P, Pruessmann KP. Electrodynamics and ultimate SNR in parallel MR imaging. Magn Reson Med 2004; 52:376–390.
13. Kaji Y, Kuroda K, Maeda T, et al. Anatomical and metabolic assessment of prostate using a 3-Tesla MR scanner with a custom-made external transceive coil: healthy volunteer study. J Magn Reson Imaging 2007; 25:517–526.
14. DeLano MC, Cooper TG, Siebert JE, Potchen MJ, Kuppusamy K. High-b-value diffusion-weighted MR imaging of adult brain: image contrast and apparent diffusion coefficient map features. AJNR Am J Neuroradiol 2000; 21:1830–1836.
15. Meyer JR, Gutierrez A, Mock B, et al. High-b-value diffusion-weighted MR imaging of suspected brain infarction. AJNR Am J Neuroradiol 2000; 21:1821–1829.
16. Burdette JH, Elster AD. Diffusion-weighted imag-

ing of cerebral infarction: are higher B values better? J Comut Assist Tomogr 2002; 26:622–627.

17. Kim HJ, Choi CG, Lee DH, Lee JH, Kim SJ, Suh DC. High-b-value diffusion-weighted MR imaging of hyperacute ischemic stroke at 1.5T. AJNR Am J Neuroradiol 2005; 26:208–215.

18. Toyoda K, Kitai S, Ida M, Suga S, Aoyagi Y, Fukuda K. Usefulness of high-b-value diffusion-weighted imaging in acute cerebral infarction. Eur Radiol 2007; 17:1212–1220.

19. O'Halloran RL, Holmes JH, Altes TA, Salerno M, Fain SB. The effects of SNR on ADC measurements in diffusion-weighted hyperpolarized He–3 MRI. J Magn Reson Imaging 2007; 185:42–49.

20. Morbach AE, Gast KK, Schmiedeskamp J, et al. Diffusion-weighted MRI of the lung with hyperpolarized helium–3: a study of reproducibility. J Magn Reson Imaging 2005; 21:765–774.

21. Dietrich O, Heiland S, Sartor K. Noise correction for the exact determination of apparent diffusion coefficients at low SNR. Magn Reson Med 2001; 45:448–453.

22. Van Zijl PC, Moonen CT, Faustino P, Pekar J, Kaplan O, Cohen JS. Complete separation of intracellular and extracellular information in NMR spectra by diffusion-weighted spectroscopy, In: Proc Natl Acad Sci USA 1991; 88:3228–3232.

23. Niendorf T, Dijkhuizen RM, Norris DG, van Lookeren Campagne M, Nicolay K. Biexponential diffusion attenuation in various states of brain tissue: implications for diffusion-weighted imaging. Magn Reson Med 1996; 36:847–857.

24. Pilatus U, Shim H, Artemov D, Davis D, van Zijl PC, Glickson JD. Intracellular volume and apparent diffusion constants of perfused cancer cell cultures, as measured by NMR. Magn Reson Med 1997; 37:825–832.

25. Mulkern RV, Gudbjartsson H, Westin CF, et al. Multi-component apparent diffusion coefficients in human brain. NMR Biomed 1999; 12:51–62.

26. Mulkern RV, Vajapeyam S, Robertson RL, Caruso PA, Rivkin MJ, Maier SE. Biexponential apparent diffusion coefficient parametrization in adult vs. newborn brain. Magn Reson Imaging 2001; 19:659–668.

27. Maier SE, Bogner P, Bajzik G, et al. Normal brain and brain tumor: multicomponent apparent diffusion coefficient line scan imaging. Radiology 2001; 219:842–849.

28. Mulkern RV, Barnes AS, Haker SJ, et al. Biexponential characterization of prostate tissue water diffusion decay curves over an extended b-factor range. Magn Reson Med 2006; 24:563–568.

Abdominal apparent diffusion coefficient measurements: effect of diffusion-weighted image quality and usefulness of anisotropic images

Takeshi Yoshikawa[a,*], Yoshiharu Ohno[a], Hideaki Kawamitsu[b], Yonson Ku[c], Yasushi Seo[d], Carlos A. Zamora[e], Nobukazu Aoyama[b], Kazuro Sugimura[a]

[a]Department of Radiology, Kobe University Graduate School of Medicine, Kobe, Hyogo 650-0017, Japan
[b]Division of Radiology, Kobe University Hospital, Kobe, Hyogo 650-0017, Japan
[c]Division of Hepato-Biliary-Pancreatic Surgery, Department of Surgery, Kobe University Graduate School of Medicine,
Kobe, Hyogo 650-0017, Japan
[d]Division of Gastrenterology, Department of Internal Medicine, Kobe University Graduate School of Medicine,
Kobe, Hyogo 650-0017, Japan
[e]Department of Radiology, San Juan de Dios General Hospital, Guatemala City 01001, Guatemala
Received 15 November 2007; revised 30 March 2008; accepted 22 April 2008

Abstract

This study aimed to assess the effect of diffusion-weighted image (DWI) quality on abdominal apparent diffusion coefficient (ADC) measurements and the usefulness of anisotropic images. Twenty-six patients (10 men and 16 women; mean, 58.1 years) who underwent DW imaging and were diagnosed not to have any abdominal diseases were analyzed. Single-shot spin-echo echo-planar DW imaging was performed, and one isotropic and three orthogonal anisotropic images were created. ADCs were calculated for liver (four segments), spleen, pancreas (head, body, tail) and renal parenchyma. Image quality for each organ part was scored visually. We estimated the correlation between ADC and image quality and evaluated the feasibility of using anisotropic images. ADCs and image quality were affected by motion probing gradient directions in the liver and pancreas. A significant inverse correlation was found between ADC and image quality. The r values for isotropic images were −.46, −.48, −.70 and −.28 for the liver, spleen, pancreas and renal parenchyma, respectively. Anisotropic images had the best quality and lowest ADC in at least one organ part in 17 patients. DWIs with the best quality among isotropic and anisotropic images should be used in the liver and pancreas.
© 2008 Elsevier Inc. All rights reserved.

Keywords: Abdomen; Apparent diffusion coefficient; Diffusion weighted; Image quality; Magnetic resonance imaging

1. Introduction

Recently, diffusion-weighted (DW) magnetic resonance (MR) imaging and measurement of apparent diffusion coefficients (ADCs) have been applied to the abdomen. The results suggest that measuring ADCs can be useful in the evaluation of diffuse liver [1–3], pancreatic [4] and renal diseases [5,6], as well as in the characterization of focal hepatic [2,7–9], pancreatic [10] and renal lesions [11].

However, image quality has suffered from blurring due to the long readout interval and from artifacts because of a high susceptibility to resonance offsets. In addition, various artifacts caused by cardiac motion and air in the lung and intestines were found to degrade image quality and diminish the reliability of ADC values in the abdominal field. Recent developments in MR units and imaging techniques have improved the quality of DW images (DWIs). However, problems still exist, especially in the left lobe of the liver and the pancreas in spite of the use of parallel imaging technique [12].

Two previous reports suggested that the use of a single motion probing gradient (MPG) direction has the potential to improve DWI quality [2,13]. However, they evaluated the differences in ADCs between isotropic and anisotropic DWIs restricted to the liver and focal hepatic lesions of patients, or to the liver, spleen, and kidney of young, healthy volunteers. Furthermore, to our knowledge, no study evaluating the correlation between abdominal ADCs and quality of DWIs has been described.

* Corresponding author. Tel.: +81 78 382 6104; fax: +81 78 382 6129.
E-mail address: yoshikawa0816@aol.com (T. Yoshikawa).

The purpose of this study was to evaluate the effect of DWI quality on ADC measurements and the feasibility of using anisotropic imaging for the assessment of DWI and ADC measurements in the abdomen.

2. Materials and methods

2.1. Patients

During a 10-month period from March 2005 to December 2005, 282 consecutive patients (185 men and 97 women; mean age, 60.7 years) suspected of having abdominal diseases underwent MR imaging with a standard protocol of our hospital that included DW imaging. The patients with obvious abdominal disorders were excluded from the study population. Twenty-six patients without evidence of diffuse or focal disease on abdominal MR images and 6- to 12-month follow-up examinations were eligible for this study (10 men and 16 women; age range, 32–71 years; mean age, 58.1 years). Our institutional review board exempted this retrospective study from requiring its participants to submit an informed consent.

2.2. Imaging technique

All MR studies were performed with a 1.5-T super-conducting imaging system (Gyroscan Intera; Philips Medical Systems, Best, The Netherlands). A body coil was used for signal transmission and a four-element phased-array body multicoil was used for reception.

All patients underwent breath-hold single-shot echo-planar DW imaging [repetition time (TR)/echo time (TE) =1500/66, matrix size=96×96 (reconstructed to 256×256), field of view=400–450 mm, number of excitations=2 (for each MPG direction), b values=0 and 600, EPI factor=33 (i.e., the number of gradient-recalled echoes per spin echo), slice thickness/gap=6/2 mm, 30 transverse slices, parallel imaging factor=3, bandwidth=32.2 kHz, selective presatura-tion using inversion recovery (SPIR) for fat saturation] in addition to a routine abdominal imaging protocol including T_1-weighted dual fast gradient-recalled echo (TR/TE=126/2.3, 4.6 ms, FA=70°, matrix size=256×196, field of view=280–350 mm, number of excitations=1, slice thick-ness/gap=8/0 mm, 30 transverse slices, parallel imaging factor=2) and T_2-weighted respiratory-triggered fast spin echo (TR/effective TE=2500/80 ms, echo train length=9, matrix size=256×196, field of view=280–350 mm, number of excitations=2, slice thickness/gap=8/0 mm, 30 transverse slices, SPIR for fat saturation, parallel imaging factor=2). The MPG pulses were applied in three orthogonal directions called P', M' and S', which are defined as P'=(−0.5x, y, z), M'=(x, −0.5y, z) and S'=(x, y, −0.5z), with x pointing from floor to ceiling, y from left to right when standing in front of the magnet and z from feet to head. Anisotropic DWIs were created for each MPG direction and were referred to P', M' and S' images, respectively. Isotropic DWIs were also created and were referred to as I images. Phase encode direction was set anteroposteriorly in all sequences. For DWI, 15 sections were obtained during a breath-hold of 15 s; hence, two sequential acquisitions were required to encompass the upper abdomen. Saturation bands were not used for DWI.

2.3. Image analysis

All ADC maps were created from I and each anisotropic image, and ADCs were calculated on a workstation with standard software (Functool and Advantage Workstation version 3.2; GE Medical Systems, Milwaukee, WI). ADCs were measured for liver (four segments), spleen, pancreas (head, body, tail) and bilateral renal parenchyma for each image by using operator-defined region-of-interest (ROI) measurements performed by the same radiologist. The ROI was an oval of 100 mm². Liver ROIs were located peripherally in each segment, and the spleen ROI was placed centrally. Vessels in the liver and spleen, as well as vessels, pancreatic duct and common bile duct in the pancreas, were avoided as much as possible. The ROI of the renal parenchyma was placed peripherally in the posterior labrum. ADCs of the cortex and medulla could not be measured separately because the matrix sizes used for the DWI were so small that it was difficult to distinguish these structures on the images. Mean ADCs were calculated for each image and compared to evaluate changes in ADC depending on the MPG direction.

Overall image quality including distortion and signal inhomogeneity on isotropic and anisotropic images was visually scored for each organ part on a three-point scale (1, organ partially or completely disappeared; 2, organ appeared heterogeneous; 3, organ appeared homogenous) on the same workstation by two experienced radiologists, who were blinded to the results of ADC measurements and recorded a consensus opinion. The average image quality scores were calculated and compared for each organ part. The number of patients in whom anisotropic images showed better quality than isotropic images was counted.

The relation between ADCs and image quality scores was evaluated for isotropic, anisotropic and overall images for each organ part.

2.4. Statistical analysis

Statistical analysis of the mean ADCs was done by one-way analysis of variance and Scheffé criterion. Statistical analysis of mean image qualities was done by the Kruskal–Wallis test and Scheffé criterion. The correlation between ADCs and image quality scores was estimated by means of the Pearson's correlation coefficient (r).

All values were expressed as mean±standard deviation. For all tests used, a P value of less than .05 was considered statistically significant.

3. Results

The left lobe of the liver was out of scan coverage in two cases, and the same is true for the spleen in one case.

Liver ADCs tended to be lower on the P′ image, except for the left medial segment, and higher on the S′ image (Fig. 1). In the right posterior segment, the difference was significant. In the spleen, ADCs tended to be lower on P′ and M′ images. ADCs in the pancreatic head and body tended to be lower on P′ and M′ images, whereas ADCs in the pancreatic tail tended to be lower on P′ and S′ images. The right and left renal parenchyma showed different trends.

For each organ part, image quality scores were best on the isotropic images (Fig. 2). However, anisotropic images had better quality than isotropic images in two cases in the right posterior lobe of the liver, in one case in the right anterior, in two cases in the left medial, in four cases in the left lateral, in one case in the spleen, in eight cases in the pancreatic head, in nine cases in the body, in five cases in the tail, in none in the right renal parenchyma and in one case in the left.

In the liver, image quality scores tended to be higher on the P′ image and lower on the S′ image, except for the left medial segment. In the spleen, scores tended to be higher on
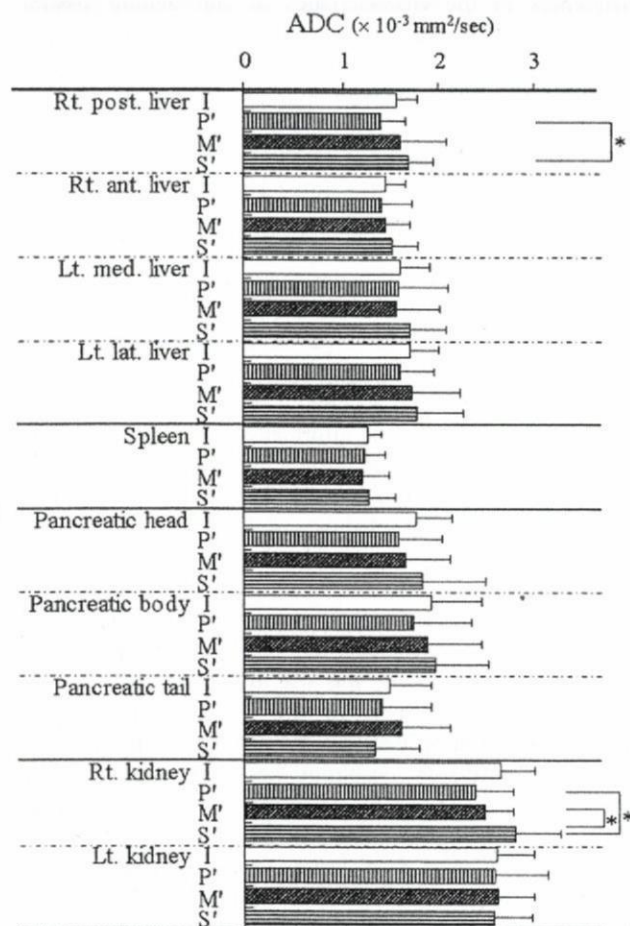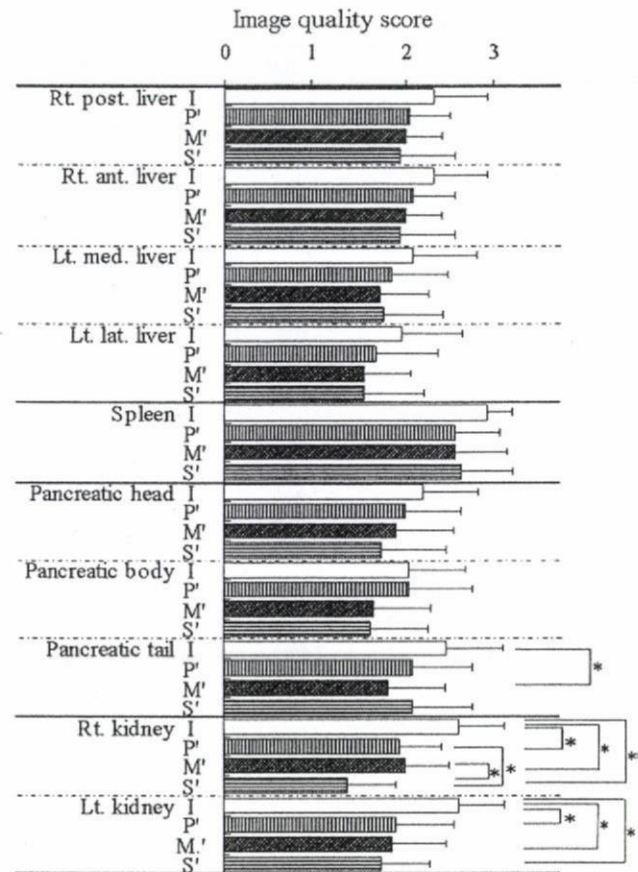

Fig. 2. Mean image quality scores for each abdominal organ part. Data are based on readers' consensus scores for DWI quality (1, poor; 2, moderate; 3, excellent). *P values are less than .05.

Fig. 1. Mean ADCs for each abdominal organ part. 'I' indicates isotropic DWIs. P′, M′ and S′ indicate anisotropic DWIs with MPG directions of $(-0.5x, y, z)$, $(x, -0.5y, z)$ and $(x, y, -0.5z)$, respectively. ant., anterior segment; med., medial segment; lat., lateral segment; lt., left; post, posterior segment; rt., right. *P values are less than .05.

P′ and M′ images. In the pancreatic head and body, scores tended to be higher on P′ and M′ images. In the pancreatic tail, scores tended to be higher on P′ and S′ images and were significantly worse on M′ images than on I images. The right and left renal parenchyma showed different trends. In the renal parenchyma, scores were significantly better on the I images.

A significant inverse correlation was found between ADC and image quality in each organ part, except for the M′ image in the spleen (Table 1). On the I images, excellent correlations were found in the pancreas and good correlations were found in the liver and spleen.

Anisotropic images had the best quality and lowest ADC in at least one organ part in 17 patients. Typical cases are shown in Figs. 3 and 4.

4. Discussion

Recent developments in MR units and imaging techniques, such as high gradient performance and parallel imaging, have improved the quality of DWIs [14]. However, there are still problems in image quality, especially in the left

Table 1
Correlation between ADCs and image quality scores

	r value	P value
Liver		
I (n=100)	−.460	<.0001
P′ (n=100)	−.506	<.0001
M′ (n=100)	−.461	<.0001
S′ (n=100)	−.507	<.0001
Overall (n=400)	−.462	<.0001
Spleen		
I (n=25)	−.483	<.05
P′ (n=25)	−.469	<.05
M′ (n=25)	−.057	>.05
S′ (n=25)	−.727	<.0001
Overall (n=100)	−.376	<.0001
Pancreas		
I (n=78)	−.701	<.0001
P′ (n=78)	−.581	<.0001
M′ (n=78)	−.623	<.0001
S′ (n=78)	−.690	<.0001
Overall (n=312)	−.625	<.0001
Renal parenchyma		
I (n=52)	−.280	<.05
P′ (n=52)	−.703	<.0001
M′ (n=52)	−.621	<.0001
S′ (n=52)	−.564	<.0001
Overall (n=204)	−.451	<.0001

'I' indicates isotropic DWIs. P′, M′ and S′ indicate anisotropic DWIs with MPG directions of $(-0.5x, y, z)$, $(x, -0.5y, z)$ and $(x, y, -0.5z)$, respectively. n, number of measurement.

lobe of the liver and pancreas [12], which may decrease the reliability of ADCs. Special techniques, such as pulse triggering or cardiac gating, have also been introduced in an attempt to improve image quality [13,14]. However, these techniques are time-consuming and limit scan coverage. In addition, the use of higher b values leads to a lower signal-to-noise ratio, resulting in insufficient image quality. Other simple techniques to improve image quality are warranted.

Isotropic images have been mainly used for abdominal DWI assessment and ADC measurements in previous researches. On the other hand, two groups of researchers suggested that the use of anisotropic images has the potential to improve the quality of DWI and the reliability of ADC. Taouli et al. [2] reported that ADCs of normal and cirrhotic liver tended to be higher on the images with y (phase-encoding) MPG direction. Another study indicated a tendency of ADCs of the liver, spleen and renal cortex to be higher on anisotropic images with M′ MPG direction [13]. However, these studies only evaluated the differences in ADCs between isotropic and anisotropic images restricted to the liver and focal liver lesions of patients [2], or to the liver, spleen, and kidney of young, healthy volunteers [13]. To our knowledge, no study evaluating the correlation between abdominal ADCs and DWI quality has been described.

In this study, we measured abdominal ADCs and scored the quality of DWI on organ parts based on isotropic and three orthogonal anisotropic images and assessed the effect of DWI quality on calculated ADCs. ADCs and image quality were affected by MPG directions in the liver and pancreas, which are thought to have isotropic diffusion because of their anatomical structures. Possible causes include characteristics of the surrounding tissues, such as air in the lung or intestine, which are considered to degrade DWI quality and decrease the accuracy of ADC. The P′ images tended to show lower ADCs and to have better quality scores in the right lobe and lateral segment of the liver and the pancreatic head and body. In these organ parts, the P′ images are thought to be less sensitive than M′ or S′ images to susceptibility artifacts from air in the lung or intestine. Cardiac motion may affect the ADCs and image quality in the medial segment of the liver. Our results suggest that the use of anisotropic images can reduce the effect of these factors. MPG direction did not affect ADCs and image quality in the spleen, possibly due to the low ADC of this organ resulting in high signal intensity on DWI. For unknown reasons, ADCs of the right and left renal parenchyma showed different trends. Small areas or number of measurement sites might be possible explanations. Differences in the characteristics of surrounding tissues should be considered. Our results could not be exactly compared to that of the two previous reports because the measurement sites in the liver were unknown in one report [13] and the MPG directions were different from those used in this study in the other [2]. However, ADCs of the liver, spleen and renal parenchyma showed similar trends to those in the study of Murtz's group.

As for the feasibility study, anisotropic images had better quality than their isotropic counterparts in the left lobe of the liver and the pancreas in a significant number of patients. The measured ADCs were lower on the ADC maps created from these anisotropic images. These results indicate that ADCs are affected by DWI quality, and images with better quality have more accurate information on diffusion in the tissues. Anisotropic images provide information in addition to isotropic images. The use of anisotropic images was thought to improve the reliability of ADCs. DWIs with the best quality among isotropic and anisotropic images should be selected for DWI assessment or ADC measurements in the liver and pancreas. However, our study could not prove the feasibility of using anisotropic images in the spleen and kidney. In these organs, the use of anisotropic images degraded image quality. In the kidney, quality was significantly better on isotropic than on anisotropic images. In addition, diffusion anisotropy has been proven in the kidney [15,16]. Therefore, DWI assessments and ADC measurements using anisotropic images should be avoided in this organ. However, focal lesions such as neoplasms are thought not to have anisotropy; therefore, our results would be applicable to focal lesions, including those in the kidney.

Our study has several limitations. First, we evaluated a small number of patients. Larger populations are needed to confirm our results. Second, we did not evaluate pathological conditions. Third, we did not obtain isotropic and anisotropic
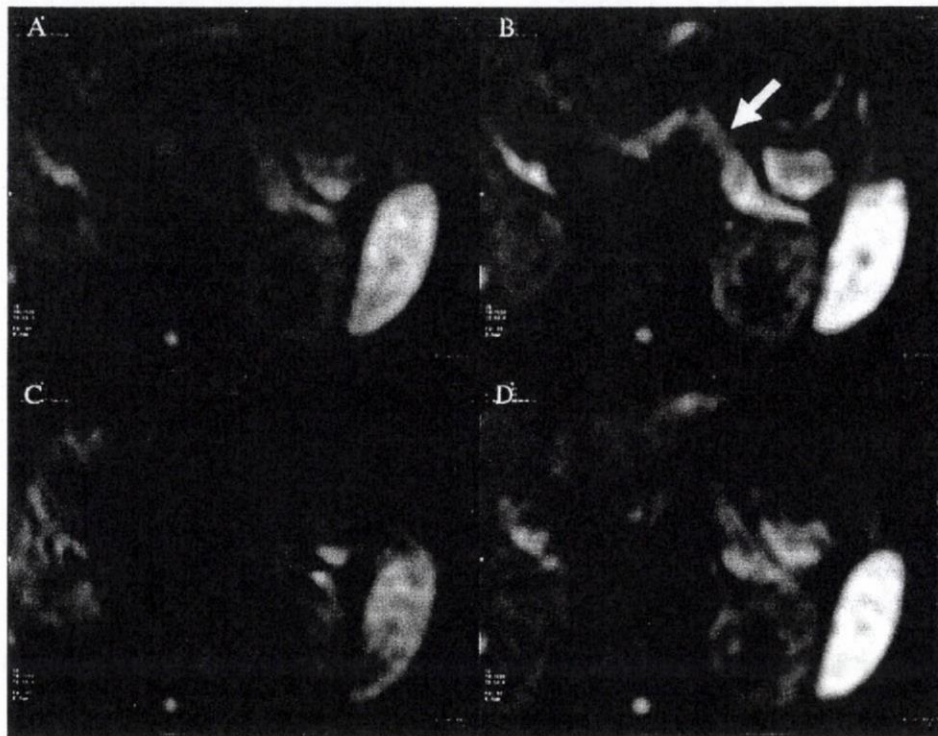
Fig. 3. A 62-year-old woman without abdominal disease. Image quality of the pancreatic body was assigned as 2 on I (A), 3 on P' (B), 1 on M' (C) and 2 on S' (D) images. ADCs in the pancreatic body are 1.95, 1.27, 2.70 and 1.74 ($\times 10^{-3}$ mm^2/s), respectively. ADC tended to decrease on the images with better quality. An arrow indicates the pancreatic body with the best image quality.
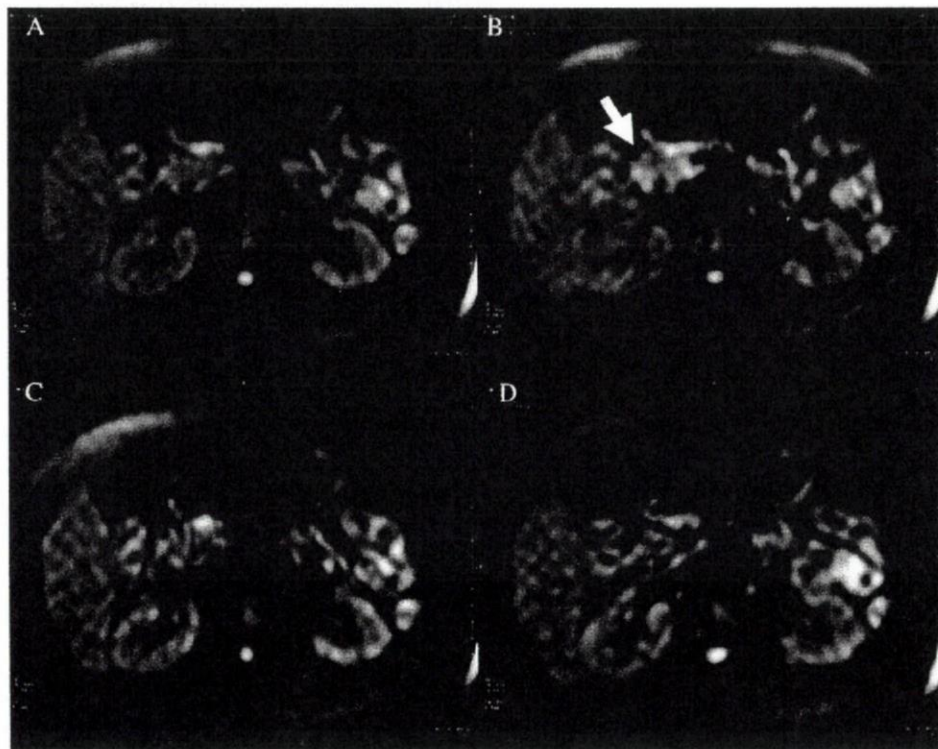

Fig. 4. A 62-year-old woman without abdominal disease. Image qualities of the pancreatic head were assigned as 2 on I (A), 3 on P' (B), 2 on M' (C) and 1 on S' (D) images. ADCs in the pancreatic head are 2.00, 1.42, 2.00 and 2.12 ($\times 10^{-3}$ mm^2/s), respectively. ADC tended to decrease on the images with better quality. An arrow indicates the pancreatic head with the best image quality.

images separately because the sites of ADC measurement or image quality scoring had to be matched among the images. As a result, the numbers of anisotropic image signal averaging were one third of those of isotropic images. This may result in underestimation of the capability of anisotropic images. In addition, only three MPG directions were evaluated in our study. In this study, M' $(x, -0.5y, z)$, P' $(-0.5x, y, z)$ and S' $(x, y, -0.5z)$ gradient pulses were applied to shorten TE. However, anisotropic images in other MPG directions might have better image quality and provide more accurate ADCs. The determination of optimal MPG directions would be difficult, because the relative positions of organ parts to the axis of the body or MR gantry vary from patient to patient. Fourth, we used a breath-hold technique only. Recently, a respiratory-triggered technique has been applied to abdominal DWI and ADC measurements [7]. Finally, interobserver variance in ADC measurements and the effects of ROI sizes in the brain have been addressed [17]. It might affect our results, especially in small organs such as the pancreas. It could affect ADC measurement in focal lesions.

5. Conclusion

Abdominal ADCs are affected by DWI quality. DWIs with the best quality among isotropic and anisotropic images should be used in DWI assessments or ADC measurements in the liver and pancreas.

Acknowledgments

References

[1] Koinuma M, Ohashi I, Hanafusa K, Shibuya H. Apparent diffusion coefficient measurements with diffusion-weighted magnetic resonance imaging for evaluation of hepatic fibrosis. J Magn Reson Imaging 2005;22:80–5.

[2] Taouli B, Vilgrain V, Dumont E, Daire JL, Fan B, Menu Y. Evaluation of liver diffusion isotropy and characterization of focal hepatic lesions with two single-shot echo-planar MR imaging sequences: prospective study in 66 patients. Radiology 2003;226:71–8.

[3] Moteki T, Horikoshi H, Oya N, Aoki J, Endo K. Evaluation of hepatic lesions and hepatic parenchyma using diffusion-weighted reordered turboFLASH magnetic resonance images. J Magn Reson Imaging 2002;15:564–72.

[4] Erturk SM, Ichikawa T, Motosugi U, Sou H, Araki T. Diffusion-weighted MR imaging in the evaluation of pancreatic exocrine function before and after secretin stimulation. Am J Gastroenterol 2006;101:133–6.

[5] Thoeny HC, De Keyzer F, Oyen RH, Peeters RR. Diffusion-weighted MR imaging of kidneys in healthy volunteers and patients with parenchymal diseases: initial experience. Radiology 2005;235:911–7.

[6] Chan JH, Tsui EY, Luk SH, Fung SL, Cheung YK, Chan MS, et al. MR diffusion-weighted imaging of kidney: differentiation between hydronephrosis and pyonephrosis. Clin Imaging 2001;25:110–3.

[7] Nasu K, Kuroki Y, Nawano S, Kuroki S, Tsukamoto T, Yamamoto S, et al. Hepatic metastases: diffusion-weighted sensitivity-encoding versus SPIO-enhanced MR imaging. Radiology 2006;239:122–30.

[8] Naganawa S, Kawai H, Fukatsu H, Sakurai Y, Aoki I, Miura S, et al. Diffusion-weighted images of the liver: comparison of tumor detection before and after contrast enhancement with superparamagnetic iron oxide. J Magn Reson Imaging 2005;21:836–40.

[9] Koh DM, Scurr E, Collins D, Kanber B, Norman A, Leach MO, et al. Predicting response of colorectal hepatic metastasis: value of pretreatment apparent diffusion coefficients. AJR Am J Roentgenol 2007;188:1001–8.

[10] Matsuki M, Inada Y, Nakai G, Tatsugami F, Tanikake M, Narabayashi I, et al. Diffusion-weighed MR imaging of pancreatic carcinoma. Abdom Imaging 2007;32:481–3.

[11] Squillaci E, Manenti G, Di Stefano F, Miano R, Strigari L, Simonetti G. Diffusion-weighted MR imaging in the evaluation of renal tumours. J Exp Clin Cancer Res 2004;23:39–45.

[12] Yoshikawa T, Kawamitsu H, Mitchell DG, Ohno Y, Ku Y, Seo Y, et al. ADC measurement of abdominal organs and lesions using parallel imaging technique. AJR Am J Roentgenol 2006;187:1521–30.

[13] Murtz P, Flacke S, Traber F, van den Brink JS, Giesecke J, Schild HH. Abdomen: diffusion-weighted MR imaging with pulse-triggered single-shot sequences. Radiology 2002;224:258–64.

[14] Taouli B, Martin AJ, Qayyum A, Merriman RB, Vigneron D, Yeh BM, et al. Parallel imaging and diffusion tensor imaging for diffusion-weighted MRI of the liver: preliminary experience in healthy volunteers. AJR Am J Roentgenol 2004;183:677–80.

[15] Fukuda Y, Ohashi I, Hanafusa K, Nakagawa T, Ohtani S, An-naka Y, et al. Anisotropic diffusion in kidney: apparent diffusion coefficient measurements for clinical use. J Magn Reson Imaging 2000;11:156–60.

[16] Ries M, Jones RA, Basseau F, Moonen CT, Grenier N. Diffusion tensor MRI of the human kidney. J Magn Reson Imaging 2001;14:42–9.

[17] Bilgili Y, Unal B. Effect of region of interest on interobserver variance in apparent diffusion coefficient measures. AJNR Am J Neuroradiol 2004;25:108–11.

Non–Small Cell Lung Cancer:

Whole-Body MR Examination for M-Stage Assessment—Utility for Whole-Body Diffusion-weighted Imaging Compared with Integrated FDG PET/CT[1]

Yoshiharu Ohno, MD, PhD
Hisanobu Koyama, MD
Yumiko Onishi, MD
Daisuke Takenaka, MD
Munenobu Nogami, MD
Takeshi Yoshikawa, MD
Sumiaki Matsumoto, MD
Yoshikazu Kotani, MD
Kazuro Sugimura, MD

Purpose: To prospectively and directly compare the capability of whole-body diffusion-weighted (DW) imaging, whole-body magnetic resonance (MR) imaging with and that without DW imaging, and integrated fluorine 18 fluorodeoxyglucose (FDG) positron emission tomography (PET)/computed tomography (CT) for M-stage assessment in non–small cell lung cancer (NSCLC) patients.

Materials and Methods: The institutional review board approved this study; informed consent was obtained from patients. A total of 203 NSCLC patients (109 men, 94 women; mean age, 72 years) prospectively underwent whole-body DW imaging, whole-body MR imaging, and FDG PET/CT. Final diagnosis of the M-stage in each patient was determined on the basis of results of all radiologic and follow-up examinations. Two chest radiologists and two nuclear medicine physicians independently assessed all examination results and used a five-point visual scoring system to evaluate the probability of metastases. Final diagnosis based on each of the methods was made by consensus of two readers. Receiver operating characteristic (ROC) analysis was used to compare the capability for M-stage assessment among whole-body DW imaging, whole-body MR imaging with and that without DW imaging, and PET/CT on a per-patient basis. Sensitivity, specificity, and accuracy were compared with the McNemar test.

Results: Area under ROC curve (A_z) values of whole-body MR imaging with DW imaging ($A_z = 0.87$, $P = .04$) and integrated FDG PET/CT ($A_z = 0.89$, $P = .02$) were significantly larger than that of whole-body DW imaging ($A_z = 0.79$). Specificity and accuracy of whole-body MR imaging with (specificity, $P = .02$; accuracy, $P < .01$) and that without DW imaging (specificity, $P = .02$; accuracy, $P = .01$) and integrated FDG PET/CT (specificity, $P < .01$; accuracy, $P < .01$) were significantly higher than those of whole-body DW imaging.

Conclusion: Whole-body MR imaging with DW imaging can be used for M-stage assessment in NSCLC patients with accuracy as good as that of PET/CT.

© RSNA, 2008

Lung cancer is the most common cause of cancer-related death among both men and women worldwide (1). Non–small cell lung cancer (NSCLC) accounts for 80% of all lung cancers, and small cell lung cancer accounts for the remainder (2). The treatment regimen for NSCLC depends on preoperative TNM staging, with curative surgical resection possible for the early stages and chemoradiotherapy, chemotherapy, or best supportive care considered advisable for the later stages, depending on the patient's performance status (3,4). Accurate tumor staging is therefore essential for choosing the appropriate treatment strategy, because it provides prognostic information and influences treatment options for patients with NSCLC.

Advances in Knowledge

- When compared with integrated fluorine 18 fluorodeoxyglucose (FDG) PET/CT on a per-patient basis, interobserver agreement and mean reading time of whole-body MR imaging with diffusion-weighted (DW) imaging were almost the same.
- A comparison of capability for M-stage assessment with the inclusion of brain metastases showed that diagnostic accuracies of whole-body DW imaging was significantly lower than that of integrated FDG PET/CT.
- A comparison of capability for M-stage assessment with the exclusion of brain metastases showed that diagnostic accuracy of whole-body DW imaging and whole-body MR imaging without DW imaging were significantly lower than that of integrated FDG PET/CT.
- If whole-body DW imaging is adopted as an adjunct for whole-body MR examination, the diagnostic capability of whole-body MR imaging for M-stage assessment can be improved, especially when evaluation of brain metastases at whole-body MR imaging is not included.

Whole-body positron emission tomography (PET) with fluorine 18 fluorodeoxyglucose (FDG) has rapidly become accepted as the standard noninvasive modality for staging lung cancer in patients. Although PET has been shown to be superior to computed tomography (CT) for the staging of lung cancer, in reality PET and CT are complementary modalities whose combined diagnostic value is superior to that of either study alone (5). In addition, technologic advances have promoted integrated PET/CT as the new modality in the arsenal of cancer staging. Given the novelty of PET/CT, the number of studies involving the comparison of PET and PET/CT of NSCLC is still limited but is growing. Studies (6–8) have revealed the superior accuracy attained with integrated PET/CT over that with PET alone for overall staging and diagnosis of NSCLC.

Whole-body magnetic resonance (MR) imaging has been put forward as another whole-body technique for the assessment of distant metastases in patients with lung cancer, as well as those with breast cancer, malignant melanoma, and pediatric and other malignancies (9–14). Advantages of whole-body MR imaging include no need for ionizing radiation exposure, information from various sequences without and with administration of contrast media, improved temporal resolution due to a newly developed parallel imaging technique, a moving table scheme

Implications for Patient Care

- Whole-body MR imaging with DW imaging can be used for M-stage assessment of patients with non–small cell lung cancer with accuracy as good as that of integrated PET/CT.
- When whole-body DW imaging is adopted as an adjunct for whole-body MR examination, the diagnostic capability of whole-body MR imaging for M-stage assessment can be improved, especially when evaluation of brain metastases at whole-body MR imaging is not included.

and/or multiple body-array coils, and suggested utility of MR imaging in various organs compared with CT and nuclear medicine studies. In addition, some investigators (15–20) have suggested that the diagnostic capability of MR imaging is equal to or better than that of standard radiologic examinations including contrast material–enhanced CT, bone scintigraphy, and/or FDG PET for the assessment of brain, bone, bone marrow, and adrenal gland metastases in oncology patients. Moreover, it has been suggested that diffusion-weighted (DW) imaging could be useful for the assessment of primary malignancy (21,22) and lymph node and/or distant metastases (23,24), as well as for detection of additional benign and/or malignant tumors (25,26), although DW imaging is widely utilized for evaluation of cerebral abnormalities (27–30). Diffusion is a physical property that describes the microscopic random movement of molecules in response to thermal energy. Also known as brownian motion, diffusion may be affected by the biophysical properties of tissues, such as cell organization and density, microstructures, and microcirculation. However, to our knowledge, no direct comparison has been made between the

use of whole-body MR imaging with DW imaging and integrated FDG PET/CT in patients with NSCLC.

In this study, we attempted to validate the hypothesis that whole-body MR imaging with DW imaging has potential as an alternative technique for the detection of distant metastases in patients with NSCLC with a capability similar to that of integrated FDG PET/CT. However, in oncology patients, utilization of FDG PET or PET/CT has been limited to assessment of brain metastases in routine clinical practice. Therefore, direct comparison of the diagnostic accuracy for M-stage assessment with the inclusion of and with the exclusion of brain metastases is important for the determination of the actual utility of whole-body MR examinations. To this end, we prospectively and directly compared the capability of whole-body MR imaging with and that without DW imaging with that of integrated FDG PET/CT for M-stage assessment with the inclusion of and with the exclusion of brain metastases in patients with NSCLC and determined the utility of whole-body DW imaging as a component of whole-body MR examination for detection of metastases.

Materials and Methods

Protocol, Support, and Funding

This prospective study was approved by the institutional review board of Kobe University Hospital and was partly supported by Eizai (Tokyo, Japan) (Y. Ohno, K.S.), Philips Medical Systems (Best, the Netherlands) (Y. Ohno, K.S.), and the Knowledge Cluster Initiative of the Ministry of Education, Culture, Sports, Science and Technology, Japan.

Subjects

All patients were enrolled after they had been properly informed and had consented to participate in this study. A total of 227 consecutive patients (118 men, 109 women; mean age, 73 years), who were referred to our hospital with a diagnosis of NSCLC at pathologic examination and who were considered candidates for surgical resection, un-

derwent prospective whole-body MR imaging with and that without DW imaging, integrated FDG PET/CT, and conventional radiologic imaging before treatment. All studies were performed in random order within 3 weeks of diagnosis and before treatment. Follow-up examinations were performed for more than 12 months after treatment.

The eventual study group of 203 patients (mean age, 72 years; age range, 47–85 years) comprised 109 men (mean age, 72 years; age range, 47–81 years) and 94 women (mean age, 72 years; age range, 49–85 years) because 24 patients were excluded due to insufficient or no follow-up examinations after treatment. The final diagnosis of NSCLC was made on the basis of findings from histologic examinations of specimens obtained by using transbronchial or CT-guided biopsy or on the basis of pathologic findings of resected specimens obtained at surgical resection at our hospital. There were 176 patients with adenocarcinomas, 19 with squamous cell carcinomas, and eight with large cell carcinomas.

Whole-Body MR Imaging

MR imaging was performed with two 1.5-T superconducting magnets (Gyroscan Intera or Achieva; Phillips Medical Systems) by using a moving tabletop and tabletop extender. A longitudinal field of view of 2000 mm and a transverse field of view of 530 mm were generated. For every examination, whole-body MR images were obtained in the coronal and sagittal planes with a body coil and a moving table. Four sequences were performed for whole-body MR imaging. One was an in-phase T1-weighted gradient-echo sequence (repetition time msec/echo time msec, 100/4.6; flip angle, 75°; 256 × 128 matrix; 512 × 256 reconstruction matrix; number of signals acquired, two), performed both with and without administration of contrast media. The second was an opposed-phase T1-weighted gradient-echo sequence (100/2.3; flip angle, 75°; 256 × 128 matrix; 512 × 256 reconstruction matrix; number of signals acquired, two) without contrast media. The third was a sequentially reordered

half-Fourier multishot short inversion time inversion recovery (STIR) turbo spin-echo sequence (3200/60/inversion time msec, 150; echo train length, 165; 256 × 128 matrix; 512 × 256 reconstruction matrix; number of signals acquired, two). The fourth was a sequentially reordered half-Fourier single-shot STIR spin-echo echo-planar imaging sequence (5759/70/180; echo train length, 141; b values, 0 and 1000 sec/mm^2; 256 × 128 matrix; 512 × 256 reconstruction matrix; number of signals acquired, four) for DW imaging. Coronal and sagittal whole-body MR studies were performed at seven contiguous stations with 32–56 consecutive 8-mm sections acquired at each station. The breath-holding technique was used for performing dual-phase T1-weighted gradient-echo and STIR sequences in the thorax, with eight sections acquired in the coronal and sagittal planes for each breath hold. During contrast-enhanced whole-body MR examination, a standard dose (0.1 mmoL per kilogram of body weight) of contrast material (gadoteridol, ProHance; Eizai) was administered intravenously through an antecubital vein. All whole-body MR examinations were performed within less than 90 minutes (mean, 75.8 minutes; examination time range, 60–90 minutes). Images acquired in matching positions were automatically aligned to generate a seamless whole-body coronal and sagittal image with the aid of commercially available software (View Forum; Philips Medical Systems) and were subjected to an interactive workstation review.

Integrated FDG PET/CT Examination for Initial Staging and Follow-up Examination

All patients fasted for at least 6 hours before intravenous administration of FDG at a rate of 3.3 MBq/kg, and images were obtained from the skull to the midthigh 60 minutes after completion of the injection. All FDG PET/CT examinations were performed with a commercially available PET/CT scanner (Discovery ST; GE Healthcare, Milwaukee, Wis). The axes of the multidetector CT and PET systems were mechanically aligned so that the patient could be moved

from the multidetector CT to the PET scanner gantry by simply changing the position of the examination table. The resulting PET and CT scans were coregistered with hardware. CT was performed from the head to the pelvic floor according to a standardized protocol with the following settings: 140 kV; 40 mA with auto mA; tube rotation time, 0.6 second per rotation; detector collimation, 16 × 1.25 mm; beam pitch, 1.675; section thickness, 3.75 mm; and reconstruction pitch, 3.27 mm (to match PET section thickness). Patients maintained normal shallow respiration during the acquisition of CT scans, and no iodinated contrast medium was administered. Immediately after unenhanced CT, PET was performed in the identical transverse field of view. The acquisition time was 2 minutes per table position.

All integrated PET/CT examinations were performed within 60 minutes. The CT data were resized from a 512 × 512 matrix to a 128 × 128 matrix to match the PET data so that the scans could be fused and CT-based transmission maps could be generated. PET data sets were reconstructed iteratively with an ordered-subsets expectation maximization algorithm and segmented attenuation correction (two iterations, 21 subsets) and with CT data. Coregistered scans were displayed by means of commercially available software (Fusion Viewer; Nihon Medi-Physics, Nishinomiya, Japan).

Conventional Radiologic Examination and Final Diagnosis of M Stage

The conventional radiologic examinations for M-stage assessment performed during the initial and the follow-up examinations included brain MR imaging with administration of contrast medium, contrast-enhanced whole-body CT, and bone scintigraphy.

The final M stage and metastasis of a given site were determined on the basis of the results of conventional radiologic, integrated FDG PET/CT, and whole-body MR examinations and on the basis of pathologic results from endoscopic, CT-guided, or surgical biopsies, as well as on the basis of results of follow-up

examinations performed for more than 12 months in every patient. The lesions suspected of being metastases on the basis of initial radiologic examination results were diagnosed as metastases when the tissues were proved to be metastatic at pathologic examination or the lesions became larger during the follow-up periods or decreased in size after treatment. The lesions suspected of being metastases on the basis of initial radiologic examination results and that could not be diagnosed as metastatic sites at pathologic examination were observed for more than 12 months and diagnosed as nonmetastatic sites when no change in size was observed during the follow-up period of more than 12 months or during treatment periods. The final determination of M stage and metastasis of a given site was made by consensus at a conference attended by diagnostic radiologists, radiation oncologists, pathologists, oncologists, and surgeons with more than 11 years of experience (range, 11–28 years).

Image Analysis

All images were interpreted by means of a picture archiving and communication system (ShadeQuest; Yokogawa Electric, Tokyo, Japan).

To determine the diagnostic capability of whole-body MR imaging with and that without DW imaging for the assessment of M stage in patients with NSCLC, all whole-body DW images and whole-body MR images obtained with and those obtained without DW imaging were prospectively and independently interpreted by two chest radiologists, one with 6 years (H.K.) and the other with 14 years of experience (Y. Ohno), in random order. Both readers were blinded to all information about the results of integrated FDG PET/CT and conventional radiologic examinations. For the assessment of the capability of whole-body DW imaging, precontrast DW images in coronal and sagittal planes (total of two sequences) were interpreted. For the assessment of the capability of whole-body MR imaging without DW imaging, pre- and postcontrast in-phase T1-weighted gradient-echo, precontrast opposed-

phase T1-weighted gradient-echo, and precontrast STIR turbo spin-echo images in coronal and sagittal planes (total of eight sequences) were interpreted. For the assessment of the capability of whole-body MR imaging with DW imaging, pre- and postcontrast in-phase T1-weighted gradient-echo, precontrast opposed-phase T1-weighted gradient-echo, precontrast STIR turbo spin-echo, and precontrast DW images in coronal and sagittal planes (total of 10 sequences) were interpreted. The presence or absence of metastases in the head and neck, thorax, abdomen and pelvis, and bone was assessed independently by the same radiologists. The probability of the presence of metastases on a per-patient basis was then evaluated with the following five-point visual scoring system: a score of 1 indicated that metastasis was definitely absent; a score of 2, probably absent; a score of 3, equivocal; a score of 4, probably present; and a score of 5, definitely present. The final determination of M stage on a per-patient basis was made by consensus of the two readers, and sites of metastases were recorded. Reading time of each MR study by each of the readers was recorded. This time was measured from the start of interpretation of images by using the picture archiving and communication system until the recording of whether a metastatic lesion was present or absent at a given site was finished.

To compare the diagnostic capability of whole-body MR imaging with and that without DW imaging with integrated FDG PET/CT for M-stage assessment, all FDG PET/CT studies were prospectively and independently interpreted by two nuclear medicine physicians with 4 and 8 years of experience, respectively (Y. Onishi and M.N.). Both readers were blinded to all information about the results of whole-body MR and conventional radiologic examinations. The presence or absence of metastases in the head and neck, thorax, abdomen and pelvis, and bone was assessed independently by the same readers. The probability of the presence of metastases on a per-patient basis was then evalu-

ated with the same five-point visual scoring system used for whole-body MR imaging. The final determination of M stage on a per-patient basis was made by consensus of the two readers, and sites of metastases were recorded. Reading time of each FDG PET/CT study by each of the readers was recorded, which was measured from the start of interpretation of images by using the picture archiving and communication system until the recording of whether a metastatic lesion was present or absent at a given site was finished.

Statistical Analysis

A κ statistic was used to determine the interobserver agreement for whole-body DW imaging, whole-body MR imaging with and that without DW imaging, and integrated FDG PET/CT on a per-patient basis. Because the P values were exploratory in nature, no Bonferroni correction was made. Interobserver agreement was considered to be slight when κ was less than 0.21, fair when κ ranged from 0.21 to 0.40, moderate when κ ranged from 0.41 to 0.60, substantial when κ ranged from 0.61 to 0.80, and almost perfect when κ ranged from 0.81 to 1.00 (31).

To compare the relative convenience of a given modality for diagnosis, the recorded reading times for both readers for each examination were averaged to determine the mean reading time of each examination per subject. The mean reading times for M-stage assessment were then compared among whole-body DW imaging, whole-body MR imaging with and that without DW imaging, and integrated FDG PET/CT by using analysis of variance followed by Tukey honestly significant difference multiple comparison testing.

To determine the feasible threshold value and capability for M-stage assessment with the inclusion of brain metastases, receiver operating characteristic (ROC) analysis was used to compare the diagnostic capability of whole-body DW imaging, whole-body MR imaging with and that without DW imaging, and integrated FDG PET/CT on a per-patient basis. This was followed by a sta-

tistical comparison of sensitivity, specificity, and accuracy by means of the Mc-Nemar test.

To determine the feasible threshold value and capability for M-stage assessment with the exclusion of brain metastases, ROC analysis was used to compare the diagnostic capability of the four methods on a per-patient basis. This was followed by a statistical comparison of sensitivity, specificity, and accuracy by means of the McNemar test.

A P value less than .05 was considered to indicate a statistically significant difference for all analyses.

Results

All whole-body MR and FDG PET/CT examinations were completed successfully without any adverse effects for any of the radiologic examinations. Representative cases are shown in Figures 1 and 2.

Details of patient characteristics are shown in Table 1. Of the 203 patients, 91 had stage I disease, 33 had stage II disease, 39 had stage III disease, and 40 had stage IV disease. Of the patients with stage IV disease, 11 patients had only bone metastases, seven patients had only lung metastases, six patients had only brain metastases, four patients had only lymph node metastases, four patients had only adrenal gland metastases, and four patients had only liver metastases, while two patients had lung, bone, and adrenal gland metastases, one patient had lung and bone metastases, and one patient had liver and abdominal lymph node metastases. Moreover, 93 sites with metastases were detected among the 203 patients with NSCLC, comprising bone metastases ($n = 29$), lung metastases ($n = 26$), lymph node metastases ($n = 13$), brain metastases ($n = 9$), adrenal gland metastases ($n = 8$), and liver metastases ($n = 8$). In addition, 156 cases with other findings were identified, including renal cysts ($n = 37$), spondylosis ($n = 25$), benign pulmonary nodules except primary lesions and lung metastases ($n = 25$), liver cysts ($n = 22$), hemangiomas in the vertebrae ($n = 13$) and liver ($n = 11$), adrenal gland adenomas

($n = 7$), compression fractures of the vertebrae ($n = 6$), pancreatic cysts ($n = 4$), colon polyps ($n = 3$), normal cervical lymph nodes showing as high-signal-intensity areas on DW images ($n = 2$), and colon cancer ($n = 1$).

Table 2 shows the results on a per-patient basis of the overall scores for assessment of probability of the presence of metastases recorded by the two readers on the basis of whole-body DW imaging, whole-body MR imaging with and that without DW imaging, and FDG PET/CT. The assessments demonstrated that interobserver agreements were substantial.

Results of comparisons of mean reading times for the four methods are shown in Figure 3. Results of analysis of variance revealed a significant difference among the mean reading times of the four methods ($F = 108.1$, $P < .001$). Mean reading times for M-stage assessment on whole-body DW images (382.4 seconds ± 177.4 [standard deviation]) and whole-body MR images obtained without DW imaging (615.6 seconds ± 284.3) were significantly shorter than those on whole-body MR images obtained with DW imaging (916.8 seconds ± 426.8, $P < .05$) and integrated FDG PET/CT images (881.6 seconds ± 419.9, $P < .05$).

The results on a per-patient basis of ROC analyses of whole-body DW imaging, whole-body MR imaging with and that without DW imaging, and FDG PET/CT for M-stage assessment inclusive of brain metastases are shown in Table 3 and Figure 4. The threshold value for the visual scoring system for each method was set at 4. A_z values for whole-body MR imaging with DW imaging ($P = .04$) and integrated FDG PET/CT ($P = .02$) were significantly larger than that for whole-body DW imaging.

Tables 3 and 4 also show the results on a per-patient basis of a comparative analysis of the diagnostic capability, including assessment of brain metastases, of whole-body DW imaging, whole-body MR imaging with and that without DW imaging, and integrated FDG PET/CT: lists of false-positive and false-negative cases for the M-stage assessment in pa-

tients with NSCLC identified by means of all four methods are included. When brain metastases were included, specificity and accuracy of whole-body MR imaging with (specificity, $P = .02$; accuracy, $P < .01$) and that without DW imaging (specificity, $P = .02$; accuracy, $P = .01$) and integrated FDG PET/CT (specificity, $P < .01$; accuracy, $P < .01$) were significantly higher than those of whole-body DW imaging. With regard to false-positive and false-negative lesions, cases differed from lesion to lesion as well as from patient to patient.
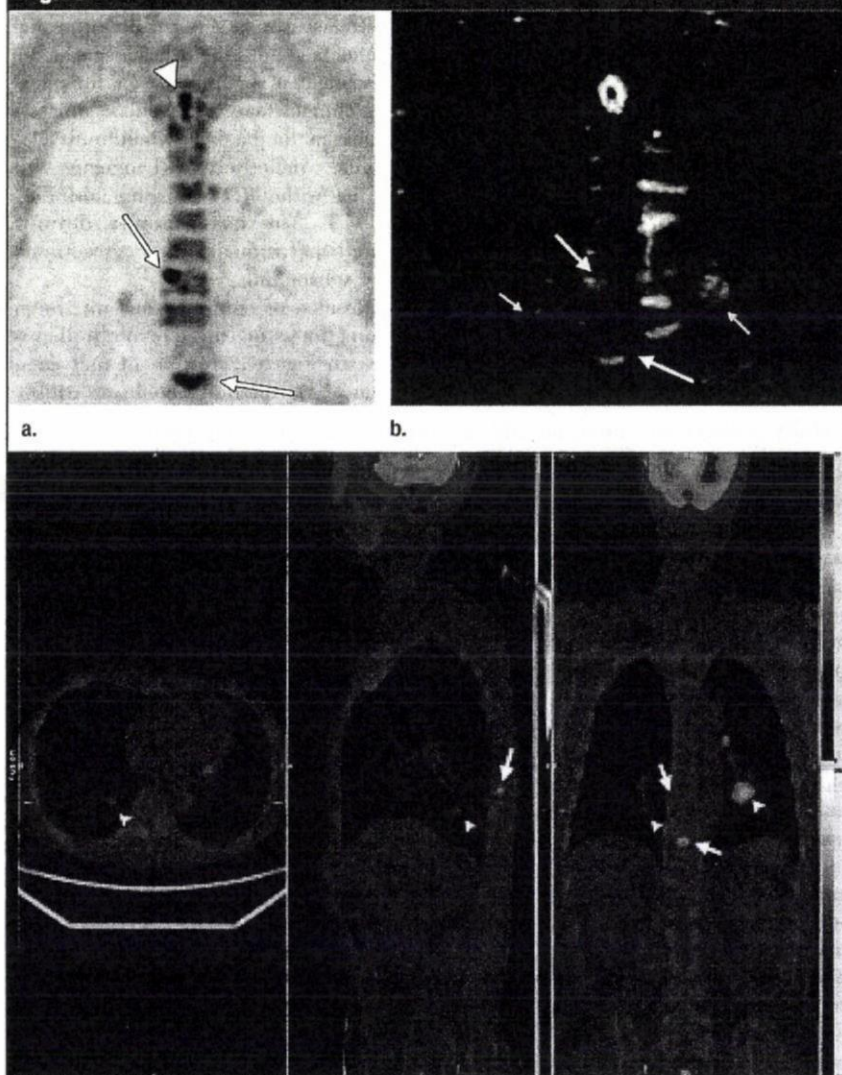
The results on a per-patient basis of ROC analyses of whole-body DW imaging, whole-body MR imaging with and that without DW imaging, and FDG PET/CT for M-stage assessment exclusive of brain metastases are shown in Table 5 and Figure 5. The threshold value for the visual scoring system for each of the methods was set at 4. A_z for integrated FDG PET/CT was significantly larger than that for whole-body MR imaging without DW imaging ($P = .03$).

The results of a comparative analysis on a per-patient basis of the diagnostic capability, with the exclusion of brain metastasis assessment, of whole-body DW imaging, whole-body MR imaging with and that without DW imaging, and integrated FDG PET/CT are also shown in Table 5. Specificity and accuracy of whole-body MR imaging with DW imaging (specificity, $P = .02$; accuracy, $P = .02$) and integrated FDG PET/CT (specificity, $P < .01$; accuracy, $P < .01$) were significantly higher than those of whole-body DW imaging. Specificity of whole-body MR imaging without DW imaging was significantly higher than that of whole-body DW imaging ($P = .02$). Accuracy of integrated FDG PET/CT was significantly higher than that of whole-body MR imaging without DW imaging ($P < .01$).

Figure 1

a.　　　　　　　　b.

c.

Figure 1: Images in 74-year-old man with adenocarcinoma, lung metastases, and bone metastases. (a) Whole-body DW image (5759/70/180) in coronal plane shows bone metastases with a score of 5 as high signal intensity (arrows). However, normal spinal cord also shows high signal intensity (arrowhead) and received a score of 5. Lung metastases within both lungs could not be detected, and areas containing these metastases were scored as 1. Although this was a true-positive case, there were two false-negative sites and a false-positive site. (b) STIR turbo spin-echo MR image (3200/60/150) in coronal plane shows lung metastases (small arrows) and bone metastases (large arrows) as high signal intensity, scored as 4 and 5, respectively. This was diagnosed as a true-positive case at whole-body MR imaging with and that without DW imaging. (c) Integrated FDG PET/CT images demonstrate bilateral lung metastases (arrowheads) and bone metastases (arrows), both of which were scored as 5. This was diagnosed as a true-positive case at integrated FDG PET/CT. Color bar = standardized uptake value, gray bar = Hounsfield units.

Discussion

Our results demonstrate that whole-body MR imaging with DW imaging can be used for M-stage assessment in patients with NSCLC with accuracy as good as that of integrated PET/CT. In addition, when whole-body DW imaging is adopted as an adjunct of whole-body MR examination, the diagnostic capability of whole-body MR examination for M-stage assessment can be enhanced, especially when evaluation of brain metastases at whole-body MR imaging is not included. After tissue diag-
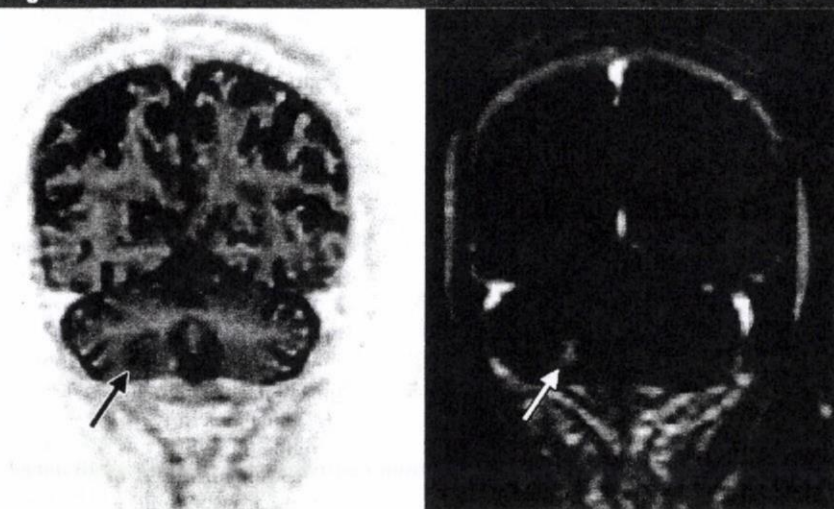
Figure 2

Figure 2: Images in 77-year-old man with adenocarcinoma and brain metastasis. Left: Whole-body DW image (5759/70/180) in coronal plane equivocally demonstrates brain metastasis, which was scored as 3, with slight high signal intensity (arrow). Right: Contrast-enhanced T1-weighted in-phase MR image (100/4.6; flip angle, 75°) in coronal plane shows brain metastasis (arrow), which was scored as 5. This was diagnosed as a false-negative case at whole-body DW imaging and as a true-positive case at whole-body MR imaging with and that without DW imaging.

Table 1

Patient Characteristics

Parameter	Datum
Age (y)	
Mean	72
Range	47–85
Sex	
Men	109
Women	94
Histologic findings	
Adenocarcinoma	176
Squamous cell carcinoma	19
Large cell carcinoma	8
Stage	
I	91
II	33
III	39
IV	40
Diagnosed metastases	
Brain metastases only	6
Lung metastases only	7
Liver metastases only	4
Adrenal gland metastases only	4
Lymph node metastases only	4
Bone metastases only	11
Lung, bone, and adrenal gland metastases	2
Lung and bone metastases	1
Liver and lymph node metastases	1
Other findings	
Cervical normal lymph nodes observed on DW image	2
Benign pulmonary nodules except primary lesions and lung metastases	25
Liver cysts	22
Hemangiomas in liver	11
Pancreatic cysts	4
Adrenal gland adenomas	7
Renal cysts	37
Hemangiomas in vertebrae	13
Compression fractures of vertebrae	6
Spondylosis	25
Colon polyps	3
Colon cancer	1

Note.—Unless otherwise indicated, data are numbers of patients.

nosis of NSCLC has been established, attention should be focused on the determination of the extent of disease, or stage. M-stage assessment is therefore important for determining the appropriate management of this disease, and integrated and/or coregistered FDG PET/CT or PET is currently in wide use.

A comparison of interobserver agreement and mean reading time for all four methods showed that interobserver agreements were almost the same and substantial on a per-patient basis. In addition, mean reading time for whole-body MR imaging with DW imaging was not significantly different from that of integrated FDG PET/CT, while mean reading times for whole-body DW imaging and whole-body MR imaging without DW imaging were significantly shorter than those for whole-body MR imaging with DW imaging and integrated PET/CT. Therefore, whole-body MR examination as a conventional screening tool for M-stage assessment in patients with NSCLC may be considered as equivalent to integrated FDG PET/CT in terms of interobserver agreement and time required.

Our results of a comparison of capability for M-stage assessment with the inclusion of brain metastases showed that A_z for whole-body DW imaging was significantly smaller than that for whole-body MR imaging with DW imaging and integrated FDG PET/CT. In addition, specificity and accuracy of whole-body DW imaging were significantly lower than those of whole-body MR imaging with and that without DW imaging and integrated FDG PET/CT. These findings suggest that whole-body DW imaging should be considered a less specific and accurate diagnostic tool than integrated FDG PET/CT for M-stage assessment in patients with NSCLC. In addition, although false-positive and false-negative cases differed from lesion to lesion and from patient to patient, lung metastases and pulmonary abnormalities and/or brain metastases accounted for the majority of false-positive and/or false-negative lesions identified with any of the four methods.

Results of previously published studies by many investigators have suggested no MR examinations of any type could have a capability for nodule detec-

tion similar to that of CT. In addition, integrated FDG PET/CT data obtained with FDG PET with free-breathing conditions, as well as data obtained with CT alone, have indicated their inferior ca-

pability for nodule detection compared with that of routine CT examination with breath holding at end inspiration (32,33). Our results are therefore compatible with these previously published results. In addition, with consideration of their capability for detection of brain metastases, detection of small metasta-

ses with whole-body DW imaging and integrated FDG PET/CT may be difficult because of the lower contrast ratio between normal cortex and brain metastases than that obtainable with contrast-enhanced MR imaging and because of the extremely high level of physiologic tissue accumulation of FDG in the cere-

bral cortex (20,34,35). Because there seems to be no significant difference in diagnostic accuracy among whole-body MR imaging with and that without DW imaging and integrated FDG PET/CT and in the diagnosis of false-positive and false-negative lesions and cases, whole-body MR imaging with and that without DW imaging can be considered as effective as integrated FDG PET/CT for M-stage assessment with the inclusion of brain metastases.

In view of the aforementioned difficulties at FDG PET or PET/CT for assessment of brain metastases (20,34, 35), the guidelines for assessment of TNM staging in NSCLC recommend that contrast-enhanced CT or MR imaging should be used instead of FDG PET or FDG PET/CT for assessment of brain metastases in routine clinical practice. Direct comparison of the diagnostic accuracy for M-stage assessment with the exclusion of brain metastases of all four methods is important for determination of the actual utility of whole-body MR examination. The results of our comparison of the diagnostic capability for M-stage assessment with the exclusion of brain metastases showed that A_z for whole-body MR imaging without DW imaging was significantly smaller than that for integrated FDG PET/CT. However, although the diagnostic performance of whole-body DW imaging for M-stage assessment—regardless of whether brain metastases are excluded or not—was lower than that of integrated FDG PET/CT, adoption of whole-body DW imaging as one of the sequences of whole-body MR examination can enhance the diagnostic accuracy of whole-body MR imaging, so that it is no longer significantly different from that of integrated FDG PET/CT. These findings indicate that whole-body DW imaging may be used to direct radiologists' attention to areas of suspected metastases but not for distinguishing malignant from benign lesions by using visual assessment of signal intensity, as was previously reported for apparent diffusion coefficient (36,37). In addition, whole-body MR imaging with DW imaging can be considered as effective for M-stage assessment as in-

Table 2

Overall Interobserver Agreement on Metastatic Probability Scores on a Per-Patient Basis for Whole-Body DW Imaging, Whole-Body MR Imaging with and That without DW Imaging, and FDG-PET/CT

Parameter	Probability Score					κ
	1	2	3	4	5	
Whole-body DW imaging						0.68
Observer 1	59	52	46	26	19	
Observer 2	60	56	56	17	14	
Whole-body MR imaging without DW imaging						0.64
Observer 1	71	49	46	20	17	
Observer 2	74	45	47	19	18	
Whole-body MR imaging with DW imaging						0.66
Observer 1	72	47	43	20	21	
Observer 2	75	44	43	18	23	
FDG PET/CT						0.68
Observer 1	87	54	28	18	16	
Observer 2	84	53	26	22	18	

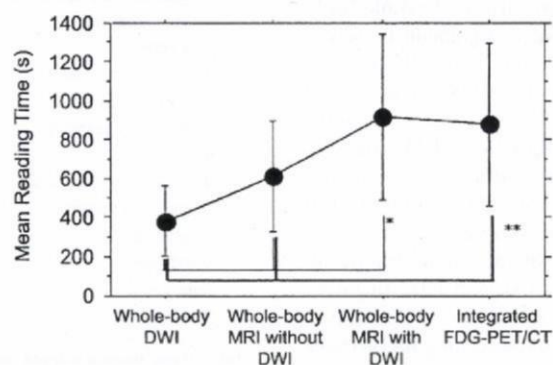Note.—Unless otherwise indicated, data are numbers of lesions.

Figure 3

Figure 3: Graph of mean reading times for whole-body DW imaging *(DWI)*, whole-body MR imaging with and that without DW imaging, and integrated FDG PET/CT. Mean reading times for M-stage assessment on whole-body DW images (382.4 seconds ± 177.4) and MR images obtained without DW imaging (615.6 seconds ± 284.3) were significantly shorter than those for whole-body MR images obtained with DW imaging (916.8 seconds ± 426.8, *P* < .05) and integrated FDG PET/CT images (881.6 seconds ± 419.9, *P* < .05). * = significant difference with whole-body MR imaging with DW imaging. ** = significant difference with integrated FDG PET/CT.

Table 3

Comparison of Diagnostic Capability on a Per-Patient Basis with Inclusion of Assessment of Brain Metastases of Whole-Body DW Imaging, Whole-Body MR Imaging with and That without DW Imaging, and Integrated FDG PET/CT

Modality	Area under ROC Curve (A_z)	Sensitivity (%)	Specificity (%)	Positive Predictive Value (%)	Negative Predictive Value (%)	Accuracy (%)
Whole-body DW imaging	0.79*†	57.5 (23/40)	87.7 (143/163)*†‡	53.5 (23/43)	89.4 (143/160)	81.8 (166/203)*†‡
Whole-body MR imaging without DW imaging	0.83	60.0 (24/40)	92.0 (150/163)	64.9 (24/37)	90.4 (150/166)	85.7 (174/203)
Whole-body MR imaging with DW imaging	0.87	70.0 (28/40)	92.0 (150/163)	68.3 (28/41)	92.6 (150/162)	87.7 (178/203)
Integrated FDG PET/CT	0.89	62.5 (25/40)	94.5 (154/163)	73.5 (25/34)	91.1 (154/169)	88.2 (179/203)

Note.—Data in parentheses are numbers used to calculate percentages.

* Significantly different from whole-body MR imaging with DW imaging ($P < .05$).

† Significantly different from integrated FDG PET/CT ($P < .05$).

‡ Significantly different from whole-body MR imaging without DW imaging ($P < .05$).
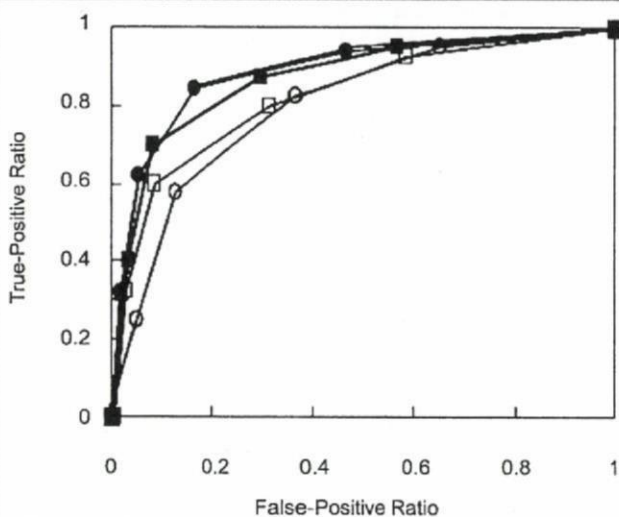
Figures 4, 5

Figure 4: Graph of ROC analyses of whole-body DW imaging (○), whole-body MR imaging with (■) and that without DW imaging (□), and integrated FDG PET/CT (●) for M-stage assessment inclusive of brain metastases on a per-patient basis in patients with NSCLC shows A_z for whole-body MR imaging with DW imaging ($P = .04$) and integrated FDG PET/CT ($P = .02$) as significantly larger than that for whole-body DW imaging.
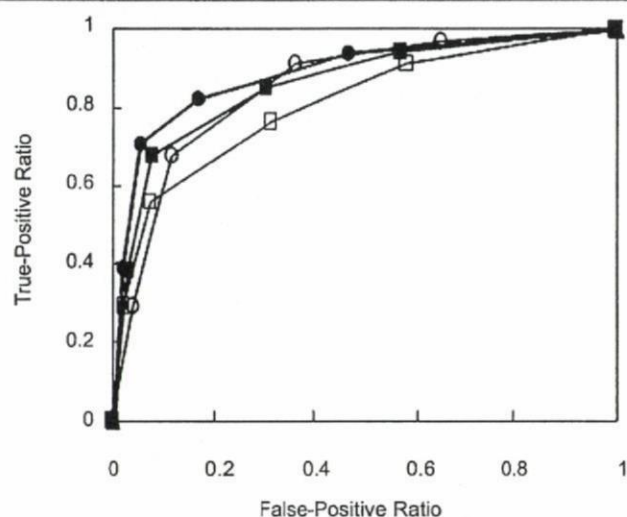
Figure 5: Graph of ROC analyses of whole-body DW imaging (○), whole-body MR imaging with (■) and that without DW imaging (□), and integrated FDG PET/CT (●) for M-stage assessment exclusive of brain metastases on a per-patient basis in patients with NSCLC shows A_z for integrated FDG PET/CT as significantly larger than that for whole-body MR imaging without DW imaging ($P = .03$).

tegrated FDG PET/CT, provided that brain metastases are excluded.

This study had certain limitations. First, previous studies have indicated that when a lung cancer reaches 5 mm in diameter, it has undergone approximately 20 doublings and contains about 100 million cells (38), while angiogenesis occurs in most tumors with a diameter of 1–2 mm (39,40). These findings

suggest that we may have missed some suspect metastatic sites that could not be detected with any of the four methods. Second, although we ensured that the final M-stage and metastasis of a given site were decided by consensus—based on the results of standard imaging; pathologic results from endoscopic, CT-guided, or surgical biopsies; and results of follow-up examinations per-

formed for more than 12 months—at a conference attended by radiologists, radiation oncologists, pathologists, oncologists, and surgeons with more than 10 years of experience, the final M stage and metastasis of a given site could not be diagnosed in every patient at pathologic examination; some sensitivity and specificity results of our study may have been biased because of incomplete

pathologic sampling. However, these limitations might bias estimates of the absolute accuracy of whole-body MR and integrated FDG PET/CT examinations, and one might expect these biases to affect both modalities relatively equally. Therefore, the difference between the modalities may be less affected by such bias.

Third, to implement whole-body MR imaging in routine clinical practice, development of a workstation and performance of further investigations for the determination of feasible sequences for whole-body MR imaging on a per-site basis may be warranted. In addition, standardization of sequences for M-stage assessment by using whole-

body MR imaging with DW imaging and improvement of MR systems for whole-body examination are necessary to adopt this method for routine clinical practice and to substitute it for integrated FDG PET/CT.

Fourth, although interobserver agreement, mean reading time, and diagnostic capability for initial M-stage as-

Table 4

False-Positive and False-Negative Cases Determined on a Per-Patient Basis with Whole-Body DW Imaging, Whole-Body MR Imaging with and That without DW Imaging, and Integrated FDG PET/CT

Modality	False-Positive Lesions	False-Negative Lesions	Other Findings
Whole-body DW imaging	Cervical lymph nodes ($n = 2$) Pulmonary abnormalities ($n = 6$) Hemangiomas in the liver ($n = 3$) Adrenal gland adenomas ($n = 1$) Hemangiomas in the vertebrae ($n = 4$) Compression fractures ($n = 4$)	Brain metastases ($n = 6$) Lymph node metastases ($n = 1$) Lung metastases ($n = 5$) Bone metastases ($n = 4$) Liver metastases ($n = 1$)	
Whole-body MR imaging without DW imaging	Pulmonary abnormalities ($n = 6$) Hemangiomas in the liver ($n = 3$) Compression fractures ($n = 4$)	Brain metastases ($n = 1$) Lymph node metastases ($n = 3$) Lung metastases ($n = 5$) Bone metastases ($n = 5$) Adrenal gland metastases ($n = 1$) Liver metastases ($n = 1$)	
Whole-body MR imaging with DW imaging	Pulmonary abnormalities ($n = 6$) Hemangiomas in the liver ($n = 3$) Compression fractures ($n = 4$)	Brain metastases ($n = 1$) Lymph node metastases ($n = 1$) Lung metastases ($n = 5$) Bone metastases ($n = 4$) Liver metastases ($n = 1$)	
Integrated FDG PET/CT	Pulmonary abnormalities ($n = 5$) Adrenal gland adenomas ($n = 2$) Compression fractures ($n = 1$) Colon polyps ($n = 1$)	Brain metastases ($n = 5$) Lung metastases ($n = 4$) Bone metastases ($n = 3$) Adrenal gland metastases ($n = 1$) Liver metastases ($n = 1$)	Colon cancer ($n = 1$)

Table 5

Comparison of Diagnostic Capability on a Per-Patient Basis with Exclusion of Assessment of Brain Metastases of Whole-Body DW Imaging, Whole-Body MR Imaging with and That without DW Imaging, and Integrated FDG PET/CT

Modality	A_z	Sensitivity (%)	Specificity (%)	Positive Predictive Value (%)	Negative Predictive Value (%)	Accuracy (%)
Whole-body DW imaging	0.85	67.6 (23/34)	87.7 (143/163)*†‡	53.5 (23/43)	92.9 (143/154)	84.3 (166/197)†‡
Whole-body MR imaging without DW imaging	0.81‡	55.9 (19/34)	92.0 (150/163)	59.4 (19/32)	90.9 (150/165)	85.8 (169/197)‡
Whole-body MR imaging with DW imaging	0.85	67.6 (23/34)	92.0 (150/163)	63.9 (23/36)	93.2 (150/161)	87.8 (173/197)
Integrated FDG PET/CT	0.89	70.6 (24/34)	94.5 (154/163)	72.7 (24/33)	93.9 (154/164)	90.4 (178/197)

Note.—Data in parentheses are numbers used to calculate percentages.

* Significantly different from whole-body MR imaging without DW imaging ($P < .05$).

† Significantly different from whole-body MR imaging with DW imaging ($P < .05$).

‡ Significantly different from integrated FDG PET/CT ($P < .05$).

sessment were compared among whole-body DW imaging, whole-body MR imaging with and that without DW imaging, and integrated FDG PET/CT, those of the above-mentioned four methods were not compared with those of each or combined standard radiologic examination. Results of a few studies (41–43) suggest that integrated PET/CT should be considered as having diagnostic accuracy equal to or higher than that of conventional radiologic imaging or PET alone in other malignancies. In addition, these study results also suggest the limitation of integrated PET/CT and the way for using it together with conventional radiologic imaging in these malignancies. Therefore, direct comparison among the above-mentioned four methods and standard radiologic examinations may also be warranted to determine the real clinical importance of whole-body MR imaging with DW imaging and integrated FDG PET/CT for M-stage assessment in patients with NSCLC. We will plan a study in the near future to prospectively and directly compare clinical utility for M-stage assessment in patients with NSCLC among whole-body MR imaging, integrated FDG PET/CT, standard radiologic examinations, and combinations of techniques discussed in this article in a large prospective cohort.

In conclusion, whole-body MR imaging with DW imaging can be used for M-stage assessment in patients with NSCLC with accuracy as good as that of integrated PET/CT; in addition, when whole-body DW imaging is adopted as an adjunct for whole-body MR imaging without whole-body DW imaging, the diagnostic accuracy of whole-body MR examination can be improved.

References

1. Parkin DM, Bray F, Ferlay J, Pisani P. Global cancer statistics, 2002. CA Cancer J Clin 2005;55:74–108.

2. Melamed MR, Flehinger BJ, Zaman MB. Impact of early detection on the clinical course of lung cancer. Surg Clin North Am 1987;67:909–924.

3. Deslauriers J. Current surgical treatment of nonsmall cell lung cancer 2001. Eur Respir J Suppl 2002;35:61s–70s.

4. Krupnick AS, Kreisel D, Hope A, Bradley J, Govindan R, Meyers B. Recent advances and future perspectives in the management of lung cancer. Curr Probl Surg 2005;42:540–610.

5. Hustinx R, Benard F, Alavi A. Whole-body FDG-PET imaging in the management of patients with cancer. Semin Nucl Med 2002;32:35–46.

6. Lardinois D, Weder W, Hany TF, et al. Staging of non-small-cell lung cancer with integrated positron-emission tomography and computed tomography. N Engl J Med 2003;348:2500–2507.

7. Cerfolio RJ, Ojha B, Bryant AS, Raghuveer V, Mountz JM, Bartolucci AA. The accuracy of integrated PET-CT compared with dedicated PET alone for the staging of patients with nonsmall cell lung cancer. Ann Thorac Surg 2004;78:1017–1023.

8. Halpern BS, Schiepers C, Weber WA, et al. Presurgical staging of non-small cell lung cancer: positron emission tomography, integrated positron emission tomography/CT, and software image fusion. Chest 2005;128:2289–2297.

9. Walker R, Kessar P, Blanchard R, et al. Turbo STIR magnetic resonance imaging as a whole-body screening tool for metastases in patients with breast carcinoma: preliminary clinical experience. J Magn Reson Imaging 2000;11:343–350.

10. Daldrup-Link HE, Franzius C, Link TM, et al. Whole-body MR imaging for detection of bone metastases in children and young adults: comparison with skeletal scintigraphy and FDG PET. AJR Am J Roentgenol 2001;177:229–236.

11. Barkhausen J, Quick HH, Lauenstein T, et al. Whole-body MR imaging in 30 seconds with real-time true FISP and a continuously rolling table platform: feasibility study. Radiology 2001;220:252–256.

12. Mazumdar A, Siegel MJ, Narra V, Luchtman-Jones L. Whole-body fast inversion recovery MR imaging of small cell neoplasms in pediatric patients: a pilot study. AJR Am J Roentgenol 2002;179:1261–1266.

13. Lauenstein TC, Goehde SC, Herborn CU, et al. Whole-body MR imaging: evaluation of patients for metastases. Radiology 2004;233:139–148.

14. Ohno Y, Koyama H, Nogami M, et al. Whole-body MR imaging vs. FDG-PET: comparison of accuracy of M-stage diagnosis for lung cancer patients. J Magn Reson Imaging 2007;26:498–509.

15. Silvestri GA, Tanoue LT, Margolis ML, Barker J, Detterbeck F; and the American College of Chest Physicians. The noninvasive staging of non-small cell lung cancer: the guidelines. Chest 2003;123(1 suppl):147S–156S.

16. Korobkin M, Lombardi TJ, Aisen AM, et al. Characterization of adrenal masses with chemical shift and gadolinium-enhanced MR imaging. Radiology 1995;197:411–418.

17. Yokoi K, Kamiya N, Matsuguma H, et al. Detection of brain metastasis in potentially operable non-small cell lung cancer: a comparison of CT and MRI. Chest 1999;115:714–719.

18. Earnest F 4th, Ryu JH, Miller GM, et al. Suspected non-small cell lung cancer: incidence of occult brain and skeletal metastases and effectiveness of imaging for detection—pilot study. Radiology 1999;211:137–145.

19. Remer EM, Obuchowski N, Ellis JD, Rice TW, Adelstein DJ, Baker ME. Adrenal mass evaluation in patients with lung carcinoma: a cost-effectiveness analysis. AJR Am J Roentgenol 2000;174:1033–1039.

20. Rohren EM, Provenzale JM, Barboriak DP, Coleman RE. Screening for cerebral metastases with FDG PET in patients undergoing whole-body staging of non-central nervous system malignancy. Radiology 2003;226:181–187.

21. Tanimoto A, Nakashima J, Kohno H, Shinmoto H, Kuribayashi S. Prostate cancer screening: the clinical value of diffusion-weighted imaging and dynamic MR imaging in combination with T2-weighted imaging. J Magn Reson Imaging 2007;25:146–152.

22. Matoba M, Tonami H, Kondou T, et al. Lung carcinoma: diffusion-weighted MR imaging—preliminary evaluation with apparent diffusion coefficient. Radiology 2007;243:570–577.

23. Abdel Razek AA, Soliman NY, Elkhamary S, Alsharaway MK, Tawfik A. Role of diffusion-weighted MR imaging in cervical lymphadenopathy. Eur Radiol 2006;16:1468–1477.

24. Nasu K, Kuroki Y, Nawano S, et al. Hepatic metastases: diffusion-weighted sensitivity-

Radiology

encoding versus SPIO-enhanced MR imaging. Radiology 2006;239:122–130.

25. Takahara T, Imai Y, Yamashita T, Yasuda S, Nasu S, Van Cauteren M. Diffusion weighted whole body imaging with background body signal suppression (DWIBS): technical improvement using free breathing, STIR and high resolution 3D display. Radiat Med 2004;22:275–282.

26. Charles-Edwards EM, deSouza NM. Diffusion-weighted magnetic resonance imaging and its application to cancer. Cancer Imaging 2006;6:135–143.

27. Schellinger PD, Fiebach JB, Hacke W. Imaging-based decision making in thrombolytic therapy for ischemic stroke: present status. Stroke 2003;34:575–583.

28. Brunel H, Girard N, Confort-Gouny S, et al. Fetal brain injury. J Neuroradiol 2004;31: 123–137.

29. Rosenbloom M, Sullivan EV, Pfefferbaum A. Using magnetic resonance imaging and diffusion tensor imaging to assess brain damage in alcoholics. Alcohol Res Health 2003;27: 146–152.

30. Lee SK, Kim DI, Kim J, et al. Diffusion-tensor MR imaging and fiber tractography: a new method of describing aberrant fiber connections in developmental CNS anomalies. RadioGraphics 2005;25:53–65.

31. Svanholm H, Starklint H, Gundersen HJ, Fabricius J, Barlebo H, Olsen S. Reproducibility of histomorphologic diagnoses with special reference to the kappa statistic. APMIS 1989;97:689–698.

32. Aquino SL, Kuester LB, Muse VV, Halpern EF, Fischman AJ. Accuracy of transmission CT and FDG-PET in the detection of small pulmonary nodules with integrated PET/CT. Eur J Nucl Med Mol Imaging 2006;33:692–696.

33. Meirelles GS, Erdi YE, Nehmeh SA, et al. Deep-inspiration breath-hold PET/CT: clinical findings with a new technique for detection and characterization of thoracic lesions. J Nucl Med 2007;48:712–719.

34. Griffeth LK, Rich KM, Dehdashti F, et al. Brain metastases from non-central nervous system tumors: evaluation with PET. Radiology 1993;186:37–44.

35. Rohren EM, Turkington TG, Coleman RE. Clinical applications of PET in oncology. Radiology 2004;231:305–332.

36. Komori T, Narabayashi I, Matsumura K, et al. 2-[Fluorine-18]-fluoro-2-deoxy-D-glucose positron emission tomography/computed tomography versus whole-body diffusion-weighted MRI for detection of malignant lesions: initial experience. Ann Nucl Med 2007;21:209–215.

37. Lichy MP, Aschoff P, Plathow C, et al. Tumor detection by diffusion-weighted MRI and ADC-mapping: initial clinical experiences in comparison to PET-CT. Invest Radiol 2007;42:605–613.

38. DeVita VT Jr, Young RC, Canellos GP. Combination versus single agent chemotherapy: a review of the basis for selection of drug treatment of cancer. Cancer 1975;35:98–110.

39. Liotta LA, Kleinerman J, Saidel GM. Quantitative relationships of intravascular tumor cells, tumor vessels, and pulmonary metastases following tumor implantation. Cancer Res 1974;34:997–1004.

40. Rak JW, St Croix BD, Kerbel RS. Consequences of angiogenesis for tumor progression, metastasis and cancer therapy. Anticancer Drugs 1995;6:3–18.

41. Gerth HU, Juergens KU, Dirksen U, Gerss J, Schober O, Franzius C. Significant benefit of multimodal imaging: PET/CT compared with PET alone in staging and follow-up of patients with Ewing tumors. J Nucl Med 2007; 48:1932–1939.

42. Tateishi U, Yamaguchi U, Seki K, Terauchi T, Arai Y, Kim EE. Bone and soft-tissue sarcoma: preoperative staging with fluorine 18 fluorodeoxyglucose PET/CT and conventional imaging. Radiology 2007;245:839–847.

43. Fonti R, Salvatore B, Quarantelli M, et al. 18F-FDG PET/CT, 99mTc-MIBI, and MRI in evaluation of patients with multiple myeloma. J Nucl Med 2008;49:195–200.